Antenna Design and Near-field Characterization for Medical Microwave Imaging Applications

João M. Felício, *Student Member, IEEE*, José M. Bioucas-Dias, *Fellow, IEEE*, Jorge R. Costa, *Senior Member, IEEE*, and Carlos A. Fernandes, *Senior Member, IEEE*

***Abstract*— In medical microwave imaging (MMWI), the antennas usually operate at close distance from the body and are required to pick up weak echoes from the inside that are masked by high skin reflection. The near-field antenna behavior strongly determines how the received signals affect the effectiveness of the imaging algorithms. However, these usually simply assume the usual antenna far-field radiation characteristics. Here, we discuss three antenna effects that can deteriorate the overall imaging performance but are rarely addressed in the literature: antenna internal reflections, angular dispersion of the "near-field phase center" and antenna frequency dispersive electric length. We propose dedicated methods to characterize these factors, and present mitigation strategies to be integrated into the inversion algorithms. We demonstrate these effects for three frequently used broadband antennas, using signals from an experimental breast imaging lab setup. In fact, the antenna study and design cannot ignore that it operates in the near-field of breast and interacts with its boundary. The methods and conclusions can be extended to other MMWI applications. To the authors' best knowledge, this is the first systematic study of the above antenna factors in the context of MMWI.**

***Index Terms*— Antenna calibration, antenna design, balanced antipodal Vivaldi antenna (BAVA), breast imaging, microwave imaging (MWI), planar monopole antenna, near-field imaging, slot antenna, ultrawideband antenna.**

I. Introduction

MICROWAVE imaging (MWI) is being studied as an complementary screening technology for medical applications, such as breast cancer screening and head hemorrhage detection [1]-[4]. It is based on monostatic or multistatic radar-type measurements, and benefits from the marked dielectric contrast between healthy and diseased tissues.

Manuscript received…

This work was partly funded by Fundação para a Ciência e Tecnologia (FCT) under projects PTDC/EEI-TEL/30323/2017 and under grant SFRH/BD/115671/2016, and by Instituto de Telecomunicações, and Universidade de Lisboa. It was also funded by FCT/MEC through national funds and co-funded by FEDER – PT2020 partnership agreement under project UID/EEA/50008/2019. This work has been developed in the framework of COST Action TD1301 (MiMed).

J. M. Felício, J. M. Bioucas-Dias and C. A. Fernandes are with Instituto de Telecomunicações, Instituto Superior Técnico (IT-IST), Universidade de Lisboa, Lisbon 1049-001, Portugal (e-mail: joao.felicio@lx.it.pt).

J. R. Costa is with Instituto de Telecomunicações, Instituto Superior Técnico (IT-IST), Universidade de Lisboa, Lisbon 1049-001, Portugal, and also with the Departamento de Ciências e Tecnologias de Informação, Instituto Universitário de Lisboa (ISCTE-IUL), Lisbon 1649-026, Portugal.

The adopted inversion algorithm is based on a method that reconstructs the reflectivity map of the volume of interest. These kinds of methods in Medical Microwave Imaging (MMWI) typically comprise two stages. The first stage aims at eliminating the strong back reflection from the skin that masks the response from the embedded tumors. This is called the skin artifact removal. The second stage aims at reconstructing the reflectivity of the inner tissues.

Antennas play an important role and strongly influence both stages of the imaging process, especially because they need to operate in close proximity of the body for link budget reasons. In fact, the faint scattered signals from tumors are additionally attenuated by the body penetration loss, while SAR considerations limit the maximum incident power. The extreme proximity of the antenna to the body requires that some otherwise overlooked antenna characteristics be properly accounted in the imaging signal post-processing.

Given that there are not many consensual near-field figures-of-merit to help in the antenna selection and design, it is not uncommon to use just far-field characteristics in the first approach. Criteria falls on phase center and radiation pattern stability, unidirectional beam [6], and phase linearity across the bandwidth [5]. Other factors that do not necessarily depend on the observation distance (but are affected by the near-field obstacles) are required as well, such as very wide impedance bandwidth, high pulse fidelity [7] and low pulse stretch. The band falls typically within the 1-10 GHz interval, as a compromise between opposing requirements: highest possible body penetration depth, highest possible image resolution, and smallest antenna size.

Frequently used antennas for MMWI seek the best compromise between the above requirements. Examples include bowties [8], [9], planar dipole- [10] and monopole [11], [12], slot-based [13], Vivaldi [14], [15] and horn [16] antennas. Another possibility to enhance antenna miniaturization is electrically short antennas backed by active circuitry [17].

In the present paper, we show that there are additional antenna factors that are quite relevant in the context of MMWI and need to be tackled. These factors can compromise the effectiveness of the skin artifact removal and image reconstruction algorithms, as will be shown ahead. We identify these factors, present methods to evaluate them and propose strategies to minimize or compensate its adverse effects on the quality of the inverted image.

The first aspect is related to internal reflections that are inherent to any antenna, regardless of its careful impedance match design. Especially with wideband antennas, it is difficult to obtain $|S_{11}(f)| \leq -15$ dB throughout the band. Even with such a low amplitude of S_{11}, this means that a non-negligible fraction of the input energy (compared to the target reflection amplitude) reflects back to the feeding port. Depending on the antenna configuration and design, these internal reflections may extend very much in time, superimposing to the echoes collected from the close body. Some algorithms do not require addressing this problem since they do not rely on the identification of the skin response (e.g. [18]); however, the same algorithms have only been proven to work with uniform breast shapes. Therefore, in realistic scenarios with non-uniform breast shapes, the internal reflections can defeat the algorithms for skin artifact removal and/or the detection of the malignancies, especially those that are close to the skin. Here, we show how the effect of mild but non-negligible internal reflections may be overcome, so that the algorithms perform accurately even in realistic examination scenarios, while having minimum impact on the backscattered echoes.

The second aspect is the "near-field phase center". Inverse imaging calculations inherently assume that the antenna phase fronts are originated at a fixed point, which is especially not true in the near-field. By studying the antenna near-field with a proposed setup, we are able to find the most representative point for the phase origin location, as well as its dependence with the incoming signal angle of arrival. We use this information to improve the imaging algorithms.

The third aspect is the electrical distance offset associated to the antenna internal flow of electric currents. We demonstrate that this distance exhibits frequency dispersive behavior. Given that MWI algorithms involve distance calculations for different frequencies, it is imperative to compensate for this dispersive offset to ensure the best image focus. We propose a procedure to calibrate the frequency-dependent offset.

We analyze the above three factors for three different antenna topologies used for MMWI: a Vivaldi-type antenna, a broadband planar monopole and a slot-based antenna, all operating in the same frequency band, Δf. The analysis is based on experimental data measured using our demonstrator for breast tumor screening. We image the breast and show that the focusing of the final image improves significantly by performing the proposed characterization of the antenna(s) and considering them in the imaging algorithm. We note that the antenna characterization strategies outlined throughout this paper are a one-time procedure, although the associated corrections need to be used for every acquired signal.

This paper is organized as follows: Section II briefly describes the antenna operation context, while Section III presents the antenna topologies that were selected for comparison. Section IV summarizes the MMWI analytical formulation; the antenna-characterization strategies to improve the performance of the algorithms and antennas are addressed in Section V; in Section VI we show the experimental application of the proposed strategies by applying them to a microwave breast imaging setup; lastly, the conclusions are drawn in Section VII.

II. Antenna Operation Context

In order to highlight the relevance of the near-field antenna characterization for MMWI, it makes sense to define a MMWI scenario as an example. This does not mean that the analysis is conditioned by the example or that the conclusion cannot be generalized for other MMWI applications.

We consider a breast cancer-screening scenario, where the patient is lying in prone position, with the breast pending in a cavity opened in the examination bed, Fig. 1 (a). The study assumes a monostatic single-antenna setup that is mechanically scanned around the breast. The variable antenna distance to the skin is d_{air}, and the distance from the ray entry-point to a generic point inside the breast is d_b. The image is reconstructed from the antenna input reflection coefficients measured at these antenna positions versus frequency, using a Vector Network Analyzer (VNA).

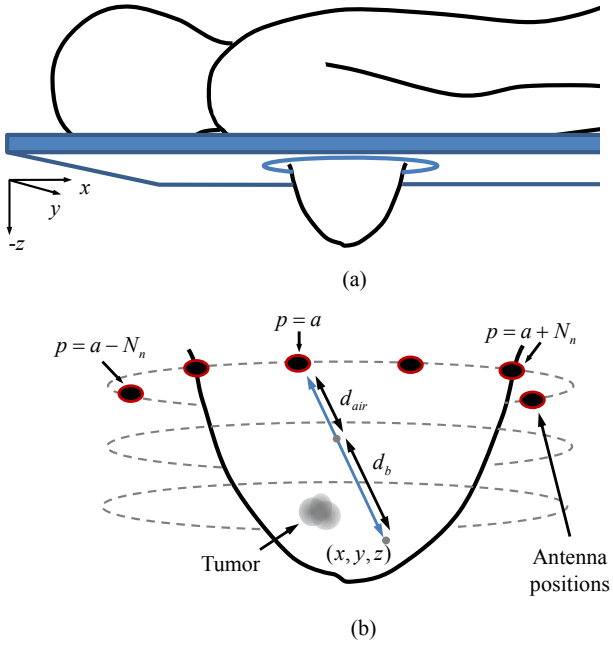

Fig. 1: (a) Breast screening scenario; (b) detail of the antenna positioning grid around the breast, and generic distances.

In the screening scenario, a three-dimensional breast shape is defined according to the ID 062204 model from the University of Wisconsin-Madison breast repository [19], derived from a MRI exam of a patient in prone posture. In the present work, we consider the breast tissue homogeneous. In the lab setup, it is a 3D-printed polylactic acid shell, (PLA, $\varepsilon_r \approx 2.75 - j0.03$ @ 4 GHz [20]), filled with a liquid of permittivity of $\varepsilon_r \approx 4 - j0.17$ at 4 GHz that emulates the breast fat tissues. The tumor is represented as a 10 mm × 20 mm ellipsoidal shape, filled with a liquid with the same dielectric properties of malignant tissues ($\varepsilon_r \approx 55 - j3$ @ 4 GHz). The recipes of both liquids are described in [21].

Unlike existing examples in the literature, no breast immersion liquid is used in this setup, in order to favor a future more practical examination scenario, comfortable and

This article has been accepted for publication in a future issue of this journal, but has not been fully edited. Content may change prior to final publication. Citation information: DOI 10.1109/TAP.2019.2905742, IEEE Transactions on Antennas and Propagation

faster for the patient, contactless and hygienic. This means that we knowingly give up the advantage of slightly lower skin contrast and potentially easier compact antenna design.

III. Antenna Topologies Under Test

Further to the already identified antenna requirements, the limited space around the breast requires that antennas are compact and low-profile. Therefore, we have considered the following candidate types for comparison: balanced antipodal Vivaldi antenna (BAVA), planar monopole antenna, and planar slot-based antenna. Optimized, compact versions of these antennas were designed using Computer Simulation Technology (CST) Transient solver [23], for an operation band defined as $\Delta f = 2-5\,\text{GHz}$.

A. Balanced antipodal Vivaldi antenna (BAVA)

Vivaldi-type antennas are widely used for MMWI, owing to its simple design and manufacturing, broadband characteristics, and reasonably unidirectional radiation [5], [14], [15]. [24]. Yet, its main drawback is the frequency dependent phase center and slightly lobulated radiation pattern. Furthermore, miniaturization is limited, although some size reduction is still achievable [25].

For this study, we used a compact BAVA, fed through a 90º bent microstrip line to minimize reflections from the outer part of the connector. The geometry of the antenna is detailed in Fig. 2. It consists of two antipodal exponential "fins" capped by truncated ellipses to achieve a compact antenna design. Two exponential curves of the form

$$\begin{cases} E_t(v) = \pm A_t \exp(P_t v) + C_t \\ E_a(u) = \pm A_a \exp(P_a u) + C_a \end{cases} \quad (1)$$

describe the "fins" and the feeding microstrip line [14] Thirteen other parameters, marked in Fig. 2, define the remainder geometry. The optimized values of coefficients A_a, C_a, P_a, A_t, C_t, and P_t are presented in TABLE I. The remaining geometry parameters are presented in TABLE II.

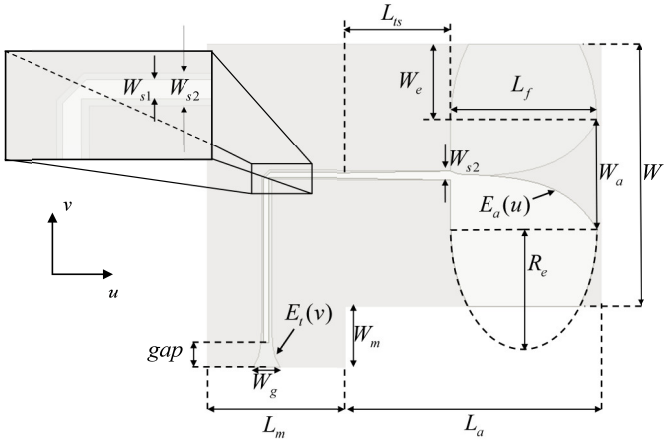

Fig. 2: Geometry and relevant parameters of the BAVA.

TABLE I

PARAMETERS OF THE EXPONENTIAL CURVES.

A_a	C_a	P_a	A_t	C_t	P_t
0.141	0.41	0.17	0.108	0.77	-0.131

TABLE II

BAVA GEOMETRY PARAMETERS DIMENSIONS IN MILLIMETERS.

W	W_a	W_m	W_g	W_{s1}	W_{s2}	W_e
44.46	28.6	10.3	8.99	0.93	1.53	13.1
L_a	L_{ts}	L_f	L_m	R_e	gap	
43.34	17.74	24.8	23.56	40.3	3.9	

The fabricated prototype is shown in Fig. 3 (a). The input reflection is bellow –15 dB in most of the band (Fig. 3 (b)), in an attempt to reduce internal reflections and increase the sensitivity to small targets. We highlight the effort undergone in order to achieve a compact design of 44.5 × 66.9 mm^2, considering that the lower frequency of operation is 2 GHz.

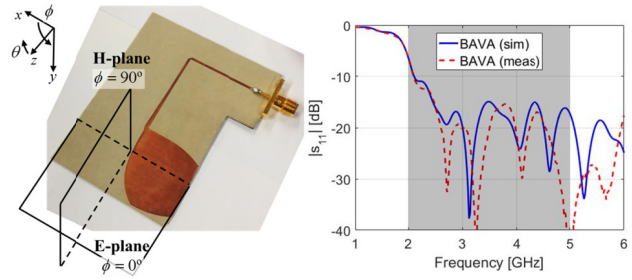

(a) (b)

Fig. 3: (a) Balanced antipodal Vivaldi antenna; (b) simulated and measured input reflection coefficient in free-space, $S_{11}^{fs}(f)$, of BAVA.

B. Planar monopole antenna

This is a very common antenna topology [7], [26], [27], including for MMWI [11]. It is easy to design, fabricate and provides a large broad frequency band. It is more straightforward to miniaturize than the Vivaldi antenna [28], [29]. The phase center is mostly stable over the lower frequency range. However, its radiation pattern is quasi-omnidirectional, and unstable at higher frequencies [30]. The designed antenna is shown in Fig. 4 (a), and the corresponding input reflection in Fig. 4 (b).

The monopole is printed on Rogers 5880 substrate (ε_r = 2.2, $tan(\delta)$ = 0.0009) of thickness of 0.254 mm (10 mils). The final area is 29 × 57.5 mm^2. The relevant dimensions are presented in TABLE III, keeping the same parameter designations as in [7].

TABLE III

DIMENSIONS OF THE PARAMETERS OF THE PLANAR MONOPOLE ANTENNA (IN MILLIMETERS).

W	L	W_1	L_1	r	h
29	57.5	0.64	23	13.8	1

The size of the ground plane of planar monopole antennas is crucial, to prevent currents from flowing into the feeding cable and re-radiating [31]. An evidence of this is the resonance near 3.9 GHz in the measured $S_{11}(f)$ in Fig. 4 (b), which is not predicted by the simulation because it did not include the measurement cable. It also has a major impact on the radiation pattern. However, we favored a compact design with small ground plane, but used a ferrite bead clamped on the measurement cable to minimize the currents flowing in the cable. The influence of the feeding cable on the antenna performance is a subject that we intentionally discuss in this

This article has been accepted for publication in a future issue of this journal, but has not been fully edited. Content may change prior to final publication. Citation information: DOI 10.1109/TAP.2019.2905742, IEEE Transactions on Antennas and Propagation

paper.

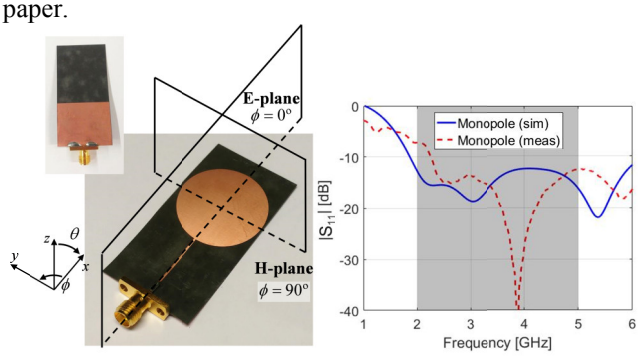

(a) (b)

Fig. 4: (a) Planar monopole antenna; (b) simulated and measured input reflection coefficient in free-space, $S_{11}^{fs}(f)$, of monopole antenna. The top left inset shows the ground plane of the monopole.

C. Planar slot-based antenna

Lastly, we used an exponentially tapered slot-based antenna of the type described in [32], in short, XETS – Fig. 5 (a). The balanced structure of the XETS provides an extremely stable phase center over the whole frequency band of operation. Furthermore, this antenna shows very good performance in both frequency- and time-domains, such as linear phase and almost flat transfer function, as well as a fidelity indicator well above 90% in the main radiation direction, offering very low pulse distortion. The radiation pattern is very stable with frequency, although quasi-omnidirectional. Many of these properties are optimum for imaging applications.

The XETS antenna was redesigned to operate in the intended band, as illustrated in Fig. 5 (b). The final antenna dimensions are presented in TABLE IV, keeping the nomenclature of the original reference [32]. The diameter of the antenna is 56 mm. It is printed on Rogers 5880 substrate of thickness of 0.254 mm.

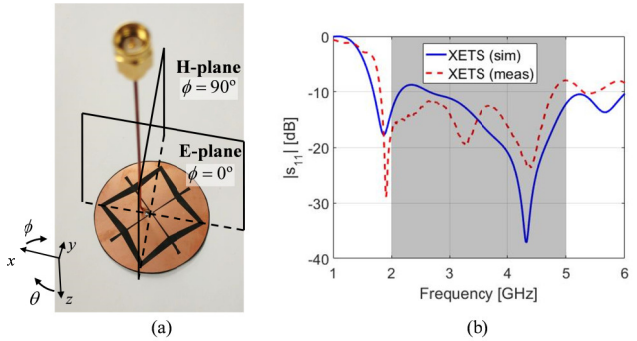

(a) (b)

Fig. 5: (a) XETS antenna; (b) simulated and measured input reflection coefficient in free-space, $S_{11}^{fs}(f)$, of XETS.

TABLE IV

Dimensions of the parameters of the XETS antenna (in millimeters).

D_{front}	D_s	L_{out}	L_{in}	w_s	w_0	L	C_0
56	52.2	35.1	26	2.9	0.21	46.9	11.7

The XETS is fed through an EZ-47 coaxial cable soldered to two opposing "petals". The unbalanced feeding marginally deteriorates the input impedance matching and the antenna performance [32]. In order to mitigate this effect, and to reduce potential pick-up from the antenna back lobe, a small absorber was clamped-on to the SMA connector.

IV. Analytical Background for MMWI

The evaluation of the antennas in the context of MMWI requires testing them together with the appropriate signal processing algorithms. This section presents the minimum information about the involved signal processing techniques that is required to understand the antenna role in this process.

A. Artifact removal

The first step before trying to reconstruct the reflectivity of the imaging domain is to eliminate the strong skin backscatter from the measured signal. This challenge is widely reported for head and breast imaging [1]-[4].

The algorithm that we use shares similarities with the Multiple Input Multiple Output (MIMO) signal processing used to separate multipath signals [22]. We use the singular value decomposition (SVD) to replace the matrix of $S_{11}(f)$ measured at different antenna positions, by an equivalent matrix representation that allows separating the contributions from the different scatterers. We assume that the different scattered signals are orthogonal and, therefore, each one is linked to a unique singular value. This allows filtering out very precisely the unwanted reflections.

Consider the geometry in Fig. 1 (b), representing the breast, and N_a uniformly distributed antenna positions in each ring. The antenna positions have index $p \in [1, N_a]$. In order to remove the dominant skin reflection as seen from an antenna at position $p = a$, we consider the input reflection of all antenna positions in the interval $a - N_n \le p \le a + N_n$, where we assume that skin reflections are similar. We assemble a $\mathbf{S}_a$ matrix, of dimension $N_f \times 2N_n + 1$,

$$\mathbf{S}_a = \left[\mathbf{s}_{a-N_n} \ \cdots \ \mathbf{s}_a \ \cdots \ \mathbf{s}_{a+N_n} \right], \tag{2}$$

where $\mathbf{s}_p = \left[S_p(f_1) \ \cdots \ S_p\left(f_{N_f}\right) \right]^T$ is a $N_f \times 1$ vector containing the antenna input reflection coefficients, measured at position p within the mentioned range, for N_f discrete frequencies distributed in the band $\Delta f = \left[f_1, f_{N_f} \right]$. The SVD matrix factorization has the form:

$$\mathbf{S}_a = \mathbf{U}\mathbf{\Sigma}\mathbf{V}^H \tag{3}$$

where $\mathbf{U}$ and $\mathbf{V}$ are orthogonal matrices, and $\mathbf{\Sigma}$ is a square diagonal matrix formed by all the singular values σ_i of $\mathbf{S}_a$ ordered in non-increasing sequence. Max$\{i\}$ is the rank of $\mathbf{S}_a$. The notation $(.)^H$ designates the Hermitian operator.

According to our formulation, reflections from the skin are well approximated by the first q singular values of $\mathbf{\Sigma}$. Therefore, provided that q can be found somehow, we can write a calibrated $\mathbf{S}_a^{cal}$ matrix free from skin reflections for the $p = a$ antenna position by subtracting from $\mathbf{S}_a$ the contribution from the unwanted q scatterers:

$$\mathbf{S}_a^{cal} = \mathbf{S}_a - \sum_{i=0}^{q} \sigma_i \mathbf{u}_i \mathbf{v}_i^H \tag{4}$$

where $\mathbf{u}_i$ and $\mathbf{v}_i$ are left- and right-singular vectors from $\mathbf{U}$ and $\mathbf{V}$, respectively. The number q is determined by testing

This article has been accepted for publication in a future issue of this journal, but has not been fully edited. Content may change prior to final publication. Citation information: DOI 10.1109/TAP.2019.2905742, IEEE Transactions on Antennas and Propagation

successively increasing values of q in equation (4), from $q = 0$ up, until a skin-reflection removal criterion is reached. This criterion is defined in the following way:

1. For each q test-value, we use the Inverse Discrete Fourier Transform (IDFT) on the vector $\mathbf{s}_a^{cal} = \left[S_a^{cal}(f_1) \;\; \cdots \;\; S_a^{cal}(f_{N_f}) \right]$ that corresponds to the antenna position $p = a$ in $\mathbf{S}_a^{cal}$, to obtain the respective spatial-domain representation $s_a^{cal}(d)$. Variable d represents the roundtrip distance to the antenna.
2. We then check if any of the relative maxima of $s_a^{cal}(d)$ falls on the distance corresponding to the entry breast skin wall $d = d_{air}$, or on the opposite wall.

If test 2) is true, then q is incremented, eq. (4) is re-calculated to remove one more singular value contribution, and we proceed to steps 1) and 2).

The process above, after finding the q that removes the skin reflection, is repeated for all N_a antenna positions, since q may change with p due to the non-uniform shape of the breast. We then assemble the matrix

$$\mathbf{S}^{cal} = \left[\mathbf{s}_1^{cal} \;\; \cdots \;\; \mathbf{s}_a^{cal} \;\; \cdots \;\; \mathbf{s}_{N_a}^{cal} \right] \tag{5}$$

where $\mathbf{S}^{cal}$ contains the calibrated signals along the frequency at each antenna position.

Our algorithm is fully automatable and compatible with real-time systems. Moreover, it works with the non-uniform shape of the breast and does not introduce distortion in the tumor position, contrarily to other algorithms found in the literature. Lastly, it has been demonstrated that the algorithm can detect tumors very close to the skin, where other methods struggle.

B. Imaging algorithm

The imaging algorithm uses the output signals from the artifact removal stage, which are organized in matrix $\mathbf{S}^{cal}$. It maps the reflectivity of the imaging domain, $r(x,y,z)$, through

$$r(x,y,z) = \frac{1}{N_a N_f} \sum_{N_a} \sum_{N_f} \mathbf{s}_a^{cal} \exp\{2jk_0 D_i\}, \tag{6}$$

where k_0 is the free-space wave-number, and the term D_i comprises the distance travelled by the propagating wave. According to Fig. 1 (b), the latter should be computed as

$$D_i = d_{air} + d_b n_b(f), \tag{7}$$

in which $n_b(f)$ is the frequency dependent refraction index of the breast tissues, and d_{air} and d_b are the straight-line distances travelled in air and through the tissues, respectively. However, in the next section, we demonstrate that D_i should include other terms that depend on the antenna but can be known *a prior* and, therefore, improve the imaging results. Lastly, the factor of 2 in the exponential argument in (6) refers to roundtrip.

Finally, the image is computed as

$$I(x,y,z) \propto \left| r(x,y,z) \right|^2. \tag{8}$$

C. Performance metrics

We use five performance metrics to assess the quality of the received signals and the image reconstruction. First, the tumor response magnitude (T) that measures the intensity of the tumor response in the final image. It indicates the amount of "useful" energy that is retrieved from the tumor. Second and third, are the tumor-to-clutter ratio (TCR) and tumor-to-mean ratio (TMR), which measure T relative to the largest and mean intensities of the background clutter, C, respectively. In log units, TCR and TMR are computed as:

$$\mathrm{TCR}[\mathrm{dB}] = 10\log_{10}\left[\max(\mathrm{T}) / \max(\mathrm{C}) \right] \tag{9}$$

$$\mathrm{TMR}[\mathrm{dB}] = 10\log_{10}\left[\max(\mathrm{T}) / \mathrm{mean}(\mathrm{C}) \right]. \tag{10}$$

We evaluate also the tumor-to-skin ratio (TSR), which indicates how much energy is coupled into the body compared to the reflection from the skin. This may be influenced by the antennas. In log units we have:

$$\mathrm{TSR}[\mathrm{dB}] = 10\log_{10}(\mathrm{T_d}/\mathrm{S_d}) \tag{11}$$

where $\mathrm{T_d}$ and $\mathrm{S_d}$ are the tumor and skin responses extracted from the spatial domain signals. This will be further developed in section VI.A.

Lastly, we calculate the tumor position error (PE), which quantifies the deviation of the detected tumor relative to the actual coordinates.

V. Analysis of the Antenna Picked-up Signals

In this section we discuss the referred three usually overlooked antenna performance aspects that influence MMWI system performance. Fig. 6 schematizes the distances involved in antenna-characterization strategies. In the scheme, vector $\mathbf{s}_a$ is the measured input reflection coefficient at position a, ρ_0 is the "near-field phase center" from which we assume the wave are radiated, and $\Delta d(\theta, \phi)$ and d^{eq} are distances that calibrate the angular dispersion of ρ_0 and radiation mechanism of the antenna, respectively. All of these parameters are defined and analyzed in this section.

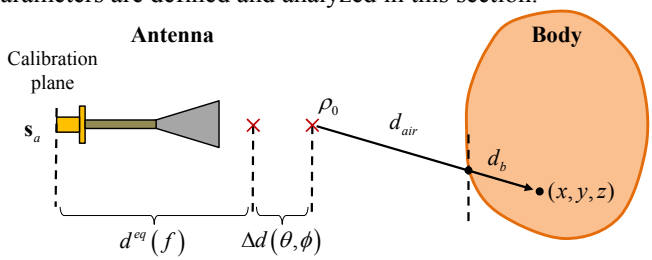

Fig. 6: Illustration of the distances involved in the antenna-calibration strategies presented ahead. The vector $\mathbf{s}_a$ corresponds to the measured input reflection coefficient at position a.

By the end of this section and according to Fig. 6, equation (7) should be modified to

$$D_i = d_b n_b(f) + d_{air} + d^{eq}(f) + \Delta d(\theta,\phi), \tag{12}$$

in order to include the calibration strategies addressed in the following sub-sections.

This article has been accepted for publication in a future issue of this journal, but has not been fully edited. Content may change prior to final publication. Citation information: DOI 10.1109/TAP.2019.2905742, IEEE Transactions on Antennas and Propagation

A. Antenna internal reflections

Regardless of how well the antennas' impedance is matched in the Δf band, the magnitude of these reflections is of the same order of magnitude as the skin backscattering and several times greater than the tumor response. Therefore, it is mandatory to eliminate this effect from the signals.

In order to comprehend the extent of this influence, let us convert the antenna free-space input reflection $S^{fs}(f)$ to the spatial-domain, $s^{fs}(d)$, using an IDFT as in Section IV.A. We just consider the frequencies within Δf (N_f = 34), and apply a Hamming window to reduce the sidelobes. The $s^{fs}(d)$ for each of the three antenna examples is shown in Fig. 7.

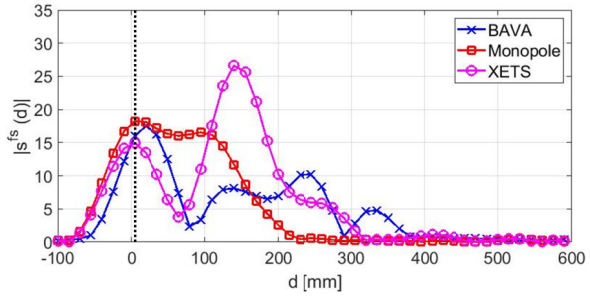

Fig. 7: Measured free-space input reflection coefficients in spatial-domain, $s^{fs}(d)$, for the three antennas considered in this study. The vertical dotted line identifies the connector-microstrip and connector-coaxial transitions at 3 mm.

Each peak corresponds to an internal reflection. It is clear that the three antennas exhibit different behaviors, apart from the common peak at $d \approx 3$ mm corresponding to the connector-microstrip or connector-coaxial cable transition. The $s^{fs}(d)$ overall relative levels in each curve are naturally related to the corresponding $S^{fs}(f)$ levels in Fig. 3 to Fig. 5.

The figure also shows that reflections extend up to approximately 300 mm. This can well superimpose on the echoes from the skin and tumors, in which case they might be shadowed. Therefore, we proceed to finding the relative importance of the skin and tumor reflections compared to the antenna internal reflections. At this point, we do not consider yet the more advanced processing from Section IV.A to highlight the physical interpretation of the results.

We consider first a healthy breast without tumor; the wall is located 20 mm away from the antenna edge. The corresponding spatial-domain antenna input reflection $s_a^{hlt}(d) = \mathrm{IDFT}\{S_a^{hlt}(f)\}$ is illustrated in Fig. 8. The vertical dashed lines identify the distances at which the breast wall reflection should be detected for each antenna (the reason why the distance is not the same is one of the main topics of the paper, and is addressed ahead).

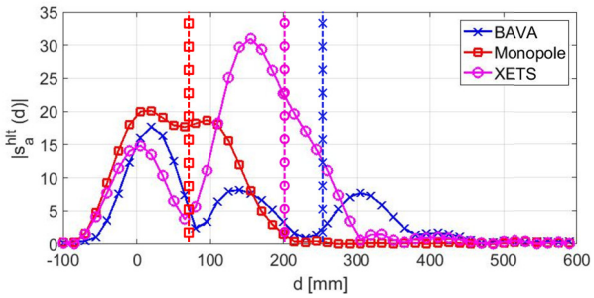

Fig. 8: Measured input reflection coefficients in the presence of the breast without tumor in spatial-domain, $|s_a^{hlt}(d)|$, for the three antennas considered in this study. The vertical dashed lines identify the distance at which the breast reflection should be detected for each antenna.

Further to a slight increase in the magnitude of the curves, compared to Fig. 7, there is no correlation between the skin position and peaks' position. These are still dominated by the antenna internal reflections. Therefore, we propose subtracting $S^{fs}(f)$ from $S_a^{hlt}(f)$ to remove its effect. This is only effective if the reflections in the antenna are immune to the presence of a dielectric body in close proximity.

The result is presented in Fig. 9, and seems to confirm the validity of the previous assumption: the skin reflection is now clearly identifiable for the three antennas, free from antenna internal reflections. The magnitude of the skin backscattering is approximately 12, 7.5 and 19 for the BAVA, monopole and XETS, respectively. The higher response from the XETS is attributed to larger aperture with significant electric field magnitude. We emphasize that the subtraction calibration strategy has minimum impact on the matching of the peaks with the corresponding vertical lines.

To conclude this analysis, we perform a similar study for the tumor. We represent in Fig. 10 the function $s_a^{tmr}(d) = \mathrm{IDFT}\{S_a^{nhlt}(f) - S_a^{hlt}(f)\}$, where $S_a^{nhlt}(f)$ is the measured antenna input reflection in front of the breast with the tumor inside.

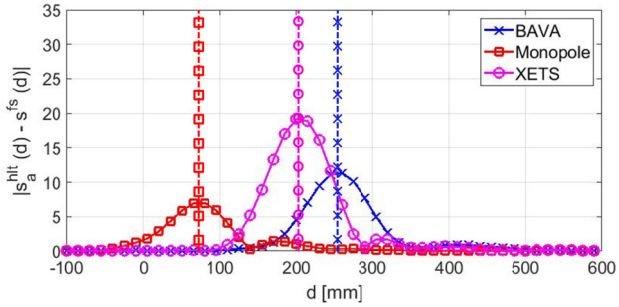

Fig. 9: Spatial-domain breast signals after subtraction of free-space reflection coefficient, $|s_a^{hlt}(d) - s_a^{fs}(d)|$, based on measured signals, for the three antennas considered in this study. The vertical dashed lines identify the distance at which the breast reflection should be detected for each antenna.

This article has been accepted for publication in a future issue of this journal, but has not been fully edited. Content may change prior to final publication. Citation information: DOI 10.1109/TAP.2019.2905742, IEEE Transactions on Antennas and Propagation

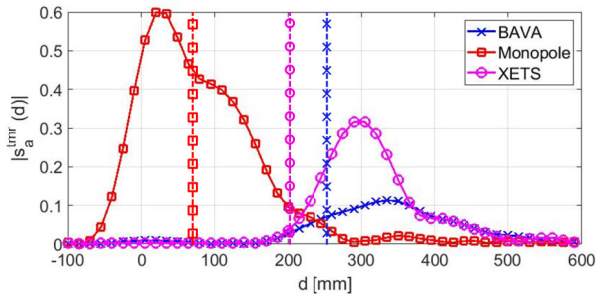

Fig. 10: Tumor response in spatial-domain, $\left|s_a^{tmr}(d)\right|$, based on measured signals, for the three antennas considered in this study. The vertical dashed lines identify the distance at which the breast reflection should be detected for each antenna.

It appears that the monopole antenna picks up the largest tumor response. However, the maximum takes place at a smaller distance than the skin reflection, which is obviously not possible. In fact, it results from the effect of the cable observed in Fig. 4. The XETS antenna detects the tumor again with the higher magnitude, 0.3 compared to 0.1 of the BAVA. Anyway, these magnitudes are nearly 60 times lower than the skin's. Both antennas show their peaks coincident with the vertical markers.

It is stressed that the employed difference-method to remove the skin is not feasible in an examination scenario, because $S_a^{nhlt}(f)$ and $S_a^{hlt}(f)$ are mutually exclusive in the same patient, by definition. However, this is possible in the lab and is enough to estimate the tumor signal characteristics just at this point of the paper, without going through the process of Section IV.

The results presented in this sub-section prove that in order to detect the skin response, we must eliminate the reflections inside the antenna. This may be achieved by subtracting S^{fs} to the input reflection coefficients in presence of the body. As a result, this strategy should precede the signal processing, when implementing an algorithm that relies on identifying the skin, as is our case as explained in Section IV.

B. Antenna "near-field phase center"

Antennas in MMWI algorithms are usually assumed as ideal point sources, located at the antenna far-field phase center position. However, in the near-field, this virtual radiation point tends to change with the observation angle. This affects the involved distance calculations, and the image focusing. Therefore, we propose to adapt the phase center concept to the near-field. Onwards, we will call it the "near-field pseudo phase center". We present a procedure to determine and characterize its dependence with the observation angle.

Consider the geometry in Fig. 11, which shows an antenna close to the breast. The shaded blue region represents the volume containing the pseudo phase center positions $\rho(\theta', \phi')$ for all observation angles θ', ϕ' in the antenna solid angle. In order to make the concept easy to apply, we define a fixed reference point within the blue region $\rho_0 = (x_0, y_0, z_0)$, such that the electric distance in equation (7) may be modified to

$$D_i = d_b n_b(f) + d_{air} + \Delta d_\rho(\theta', \phi'), \qquad (13)$$

where $d_b + d_{air}$ is the distance between the test point (x, y, z) and ρ_0, and the additional term $\Delta d_\rho(\theta', \phi')$, the distance between $\rho(\theta', \phi')$ and ρ_0, accounts for the angular dispersion of the pseudo phase center relative to ρ_0. Note that angle θ' in Fig. 12 is defined in spherical coordinates between the test point, (x, y, z), and ρ_0. The ϕ' angle (not shown) corresponds to the other spherical coordinate angle.

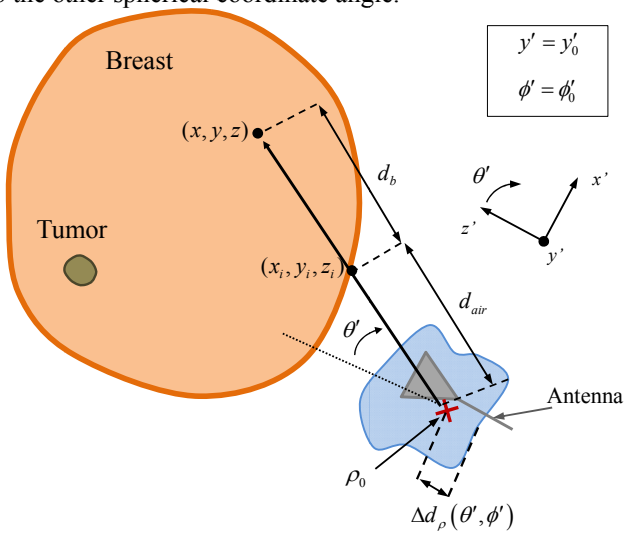

Fig. 11: Representation of the pseudo phase center, $\rho(\theta', \phi')$, and variation with angles θ' and ϕ' in 2D geometry. The irregular blue shape represents the volume containing $\rho(\theta', \phi')$.

It remains to discuss the determination of ρ_0 and $\Delta d_\rho(\theta', \phi')$. To this end, we assembled the setup depicted in Fig. 12, in which the static antenna radiates in the +z-direction towards a metallic sphere with coordinates (x_s, y_s, z_s). The latter sweeps the xy-plane with constant z_s. At each position, we measure the input reflection coefficient, $S_s(f)$, which captures the response of the sphere. We then convert $S_s(f)$ to the spatial domain, $s_s(d)$, and subtract $s^{fs}(d)$. This allows inferring the electrical distance d'_s at which the target is detected. For each antenna, the reference point (0, 0, 0) is assumed to be at the physical aperture of the antenna.

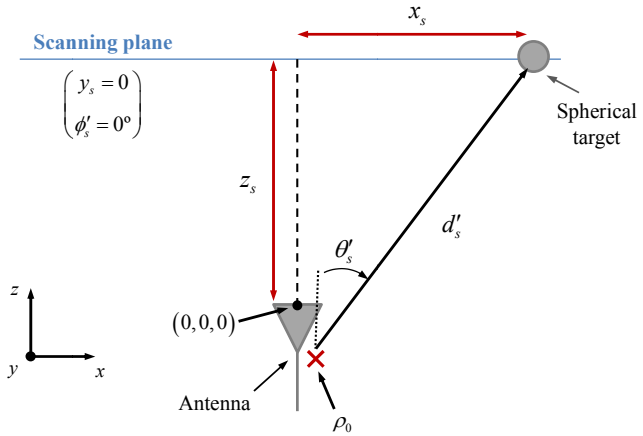

Fig. 12: Two-dimensional schematic representation of the measurement setup used to characterize the "near-field phase center", $\rho(\theta, \phi)$. The actual setup is three-dimensional, with a similar representation in the yz-plane.

This article has been accepted for publication in a future issue of this journal, but has not been fully edited. Content may change prior to final publication. Citation information: DOI 10.1109/TAP.2019.2905742, IEEE Transactions on Antennas and Propagation

The coordinates of ρ_0 are determined as the average coordinates of the pseudo phase center in both E- and H-planes of the antenna (see Figs. 2 – 4):

$$\rho_0 = \frac{1}{2}\left(\rho_E + \rho_H\right). \tag{14}$$

In turn, ρ_E and ρ_H are computed as the ρ_0 value that minimizes the following least-square problems:

$$\rho_E = \min_{\theta_s \le \theta'_{\max}} \left\{ \sqrt{\sum_{\theta_s} \left[d'_s\left(\theta'_s, \phi'_s = 0^\circ\right) - d^{avg}_{s,E}\left(\theta'_s, \phi'_s = 0^\circ\right)\right]^2} \right\} \tag{15}$$

$$\rho_H = \min_{\theta_s \le \theta'_{\max}} \left\{ \sqrt{\sum_{\theta_s} \left[d'_s\ \left(\theta'_s, \phi'_s = 90^\circ\right) - d^{avg}_{s,H}\left(\theta'_s, \phi'_s = 90^\circ\right)\right]^2} \right\} \tag{16}$$

in which d'_s is the distance between the ρ_0 under test and the target, $d^{avg}_{s,E}\left(\theta'_s, \phi'_s = 0^\circ\right)$ and $d^{avg}_{s,H}\left(\theta'_s, \phi'_s = 90^\circ\right)$ are the average values of the measured d'_s in each plane, restricted to some angular interval of interest $\theta'_{\max} \le 30^\circ$.

It is noted that, in the way they were defined, neither ρ_0 nor $\Delta d_\rho\left(\theta', \phi'\right)$ depend explicitly on frequency, rather they incorporate it through the IDFT.

As an example, the pseudo phase center is calculated for the previous three test antennas, using a 7 mm metallic sphere in air as target, at constant $z_s = \lambda_3 = 100$ mm (where λ_3 is the free-space wavelength at 3 GHz) from the antenna. The linear scan of the target was performed using a Bosch Rexroth XZ linear positioner. The sweep extended from -175 mm up to 175 mm in steps of 5 mm in both *x* and *y* directions.

We present in TABLE V the coordinates of the reference point ρ_0 obtained in the referred test, considering $\theta'_{\max} = 30^\circ$. Moreover, Fig. 13 shows $\Delta d_\rho(\theta', \phi')$ over the entire scanning plane for the three antennas, after interpolating over a regular grid. For some angles using the monopole antenna, the target was not detected and so $\Delta d_\rho(\theta', \phi')$ could not be inferred.

TABLE V

Near-field phase centers, ρ_0, of the three antennas calculated using the proposed method, for $\theta'_{\max} = 30^\circ$. The center of the reference frame is assigned in Fig. 12.

	BAVA	***Monopole***	***XETS***
ρ_0 (*x*, *y*, *z*) [mm]	(-10, 0.5, -24.5)	(-7.5, 0, -5)	(-0.5, 0.5, -13)

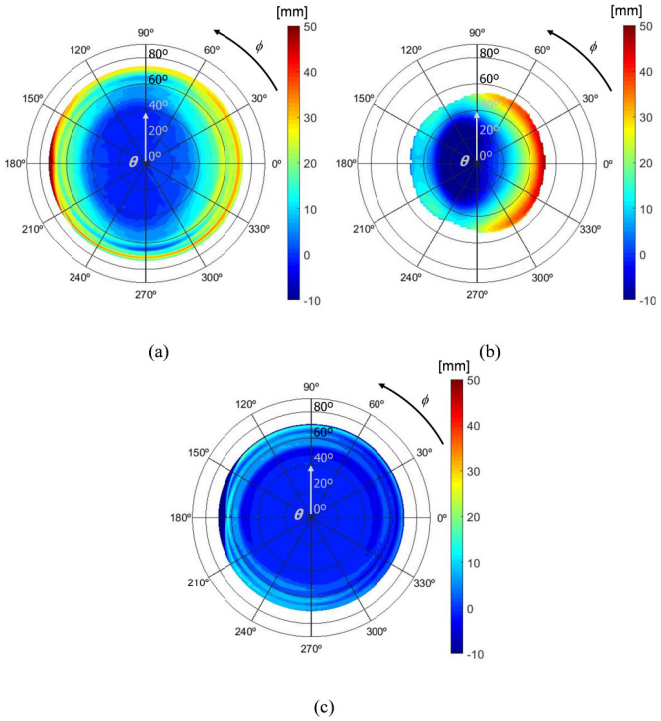

Fig. 13: Variability of near-field phase center over angle, $\Delta d_\rho(\theta, \phi)$, for the three antennas over the entire scanning plane: (a) BAVA; (b) monopole antenna; (c) XETS antenna. The radial angle is theta and the polar angle is phi.

In the E-plane, both BAVA and XETS antennas present very stable phase centers in the interval between $\theta'_{\max} \le 30$ which is relatively broad. Concerning the monopole, the phase center is very unstable due to the measurement cable (this result justifies the option of restricting the calculation of ρ_0 to $\theta'_{\max}$). In fact, for angles broader than $\theta'_{\max} > 45^\circ$ the target was very often not detected. In the H-plane, the three antennas have reasonably stable phase center up to $\theta'_{\max} \le 25^\circ$, but, again, BAVA and XETS have the best performance. We note that the phase center of the monopole antenna is more stable in the H-plane than in the E-plane, since the influence of the cable is the same for all angles.

The $\Delta d_\rho(\theta', \phi')$ information for the tested solid angle can be stored as a lookup table for proper distance correction in equation (12), for the image inversion. An experimental example of this strategy will be presented in Section VI.

C. Antenna offset length

As observed in the section V, although the measurements were done in the exact same conditions, the skin reflection does not occur at the same distance for all antennas (recall Fig. 9). Indeed, as the electric currents propagate on the antenna, they add an offset length that depends on the antenna geometry and operation mode (e.g. phase center and feeding cable). It is crucial to account for this additional length in MMWI; otherwise, the final image will not be properly focused, leading to inaccurate results. Moreover, the offset length exhibits frequency-dependent variation, whereby taking an average value may be the simplest solution, but it is certainly not the most accurate. Despite being a critical procedure, this subject is rarely addressed. For instance, in [5]

the authors propose a two-stage calibration technique involving reference targets. However, it does not account for the frequency dependency of the electrical length. In this section, we show how to calculate the electrical length of any antenna. All calculations in this section are referred to the pseudo phase center data computed in the previous section.

Let us designate the frequency-dependent offset length introduced by the *i*-th antenna as $d_i^{eq}(f)$ and $d_{ij}^{eq}(f)=d_i^{eq}(f)+d_j^{eq}(f)$ as the offset length introduced by the Tx and Rx antennas relative to their "near-field phase center", $\rho_{0,i}$. Note that $d_i^{eq}(f)$ is actually an electrical length, since we consider the propagation speed as being the speed of light in vacuum.

It is known that the phase of a transmission coefficient between two antennas *i* and *j*, $S_{ij}(f)$, is related to the distance between the antennas through:

$$\arg\{S_{ij}(f)\}=-nk_0(f)d_{total} \tag{17}$$

where n is the refractive index of the medium between the antennas, k_0 is the free-space wavenumber and d_{total} is the electrical distance between the two calibration ports. In fact, d_{total} can be decomposed into three terms corresponding to the Tx and Rx antennas and the physical distance, d:

$$\arg\{S_{ij}(f)\}=-k_0(f)\left[d+\underbrace{d_i^{eq}(f)+d_j^{eq}(f)}_{d_{ij}^{eq}(f)}\right]. \tag{18}$$

We can use this information to infer $d_{ij}^{eq}(f)$ as

$$d_{ij}^{eq}(f)=-\frac{\arg\{S_{ij}(f)\}}{k_0(f)}-d. \tag{19}$$

In order to fully characterize the offset length this method requires at least two antennas, if they are considered identical. As this is rarely true, we formulate the method for three antennas. To this end, we measure the transmission coefficients between the pairs of antennas, as sketched in Fig. 14.

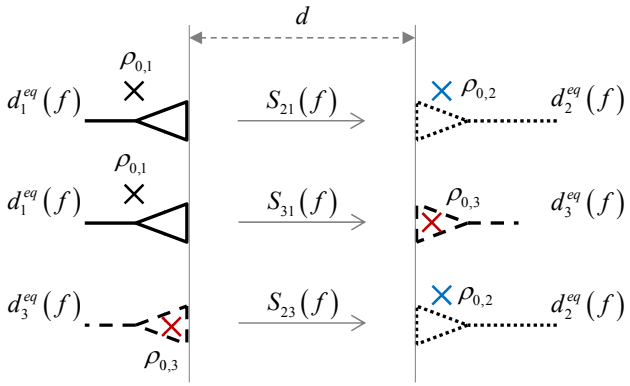

Fig. 14: Representation of the measurement setup used to calculate the equivalent length introduced by the antennas, based on the transmission coefficients.

We end up having three unknown offset distances: $d_1^{eq}(f)$, $d_2^{eq}(f)$ and $d_3^{eq}(f)$. Through relation (19) we calculate $d_{12}^{eq}(f)$, $d_{13}^{eq}(f)$ and $d_{23}^{eq}(f)$, from which we infer

$$\begin{cases} d_1^{eq}(f)=\frac{1}{2}\left[d_{21}^{eq}(f)+d_{31}^{eq}(f)-d_{32}^{eq}(f)\right] \\ d_2^{eq}(f)=d_{21}^{eq}(f)-d_1^{eq}(f) \\ d_3^{eq}(f)=d_{31}^{eq}(f)-d_1^{eq}(f) \end{cases}. \tag{20}$$

In order to calibrate the offset distance, one needs only to compensate for the phase delay corresponding to $d_i^{eq}(f)$ prior to post-processing signals, as denoted by the term $d^{eq}(f)$ in (12).

We applied the equivalent-length calibration method to the three antennas included in this study. In our measurement setup, we set d = 119 mm. The calculated distances are shown in Fig. 15 along the frequency range of 2 GHz up to 5 GHz.

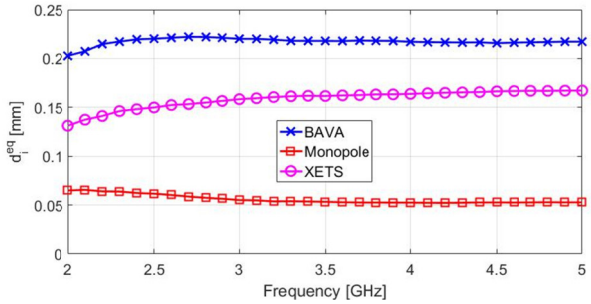

Fig. 15: Equivalent offset distance, $d_i^{eq}(f)$, over the 2-5 GHz frequency spectrum for the three antenna topologies considered in this study.

The BAVA and XETS antennas have the largest equivalent distance because of the feeding microstrip and cable, respectively. As for the monopole, it is fed by the connector and the microstrip length is shorter. Fig. 15 shows a maximum-to-minimum variation of 19.7 mm (0.23λ_c, where λ_c corresponds to the free-space wavelength at f_c = 3.5 GHz) along frequency for the BAVA, 13.6 mm (0.16λ_c) for the monopole, and of 36.3 mm (0.42λ_c) for the XETS. If ones takes the average value of $d_i^{eq}(f)$, the error introduced in the distance calculation at each frequency may be significant and lead to lower quality focusing.

As an example of the importance of calibrating the equivalent offset distance, we illustrate $\left|s_a^{hlt}(d)-s_a^{fs}(d)\right|$ and $\left|s_a^{tmr}(d)\right|$ in Fig. 16 and Fig. 17, respectively, after the equivalent distances were calibrated.

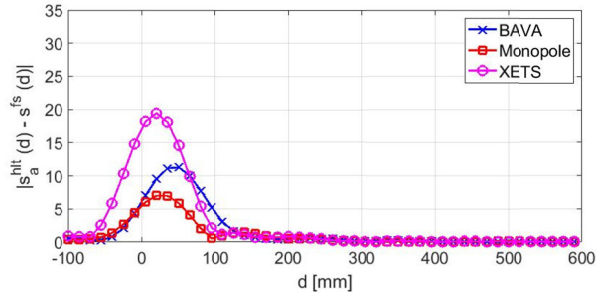

Fig. 16: Spatial-domain signals after subtraction of free-space reflection coefficient and equivalent distance calibration, $\left|s_a^{hlt}(d)-s_a^{fs}(d)\right|$, based on measured signals, for the three antennas considered in this study.

This article has been accepted for publication in a future issue of this journal, but has not been fully edited. Content may change prior to final publication. Citation information: DOI 10.1109/TAP.2019.2905742, IEEE Transactions on Antennas and Propagation

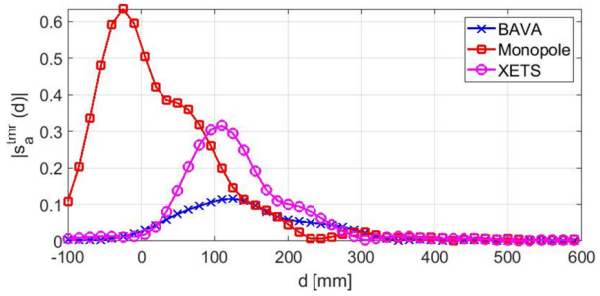

Fig. 17: Tumor response in spatial-domain, $\left|s_a^{tmr}(d)\right|$, after equivalent distance calibration, based on measured signals, for the three antennas considered in this study.

We verify that after the equivalent distance is calibrated, the peaks are aligned and correspond to the actual separation between antenna and skin for the three antennas. These results compare with Fig. 9. Although the results illustrated in Fig. 16 and Fig. 17 were obtained in similar measurement conditions, in particular the physical distance between the antenna and the breast was kept the same, we can observe that the skin and tumor backscattering are not obtained at the same distance for the three antennas. This is a consequence of the location of the pseudo phase center (recall TABLE V), which is different for the three antennas (and therefore the skin and tumor are detected at different distances).

VI. Experimental Imaging Results

This section compares the imaging results obtained with the three antennas, tested under the same experimental setup conditions, using all the previously presented correction factors. Referring to Fig. 1, we adopted a 60 mm radius for the three antenna circular paths, each one comprising 24 antenna measurement positions each, separated by 15 degrees (N_a = 72). The rings were positioned at z = -33 mm, z = -43 mm and z = -53 mm (the breast has negative z coordinates).

A. Energy coupling into breast

In sections V.A and V.C we verified that the XETS antenna retrieved the largest tumor response of the three antennas (Fig. 17). Nevertheless, we also observed that the skin backscattering was larger for the XETS (Fig. 16). Recall that in these results the higher value presented for the monopole is a consequence of the feeding cable and does not correspond to the tumor. As a result, we cannot conclude that the slot-based antenna favors the tumor response relative to the skin backscattering.

So, in order to understand which antenna couples more energy into the breast, we calculated the TSR for each of the three antennas under similar measurement conditions over a complete spatial scan around the breast. The maximum magnitude tumor response, T_d, is calculated from $\left[s_a^{tmr}(d)\right]^2$ and S_d is calculated from $\left[s_a^{hlt}(d) - s_a^{fs}(d)\right]^2$. The TSR results are presented in Fig. 18. The absent markers for the monopole antenna correspond to positions where the feeding cable precludes the detection of the tumor response (see for instance Fig. 17).

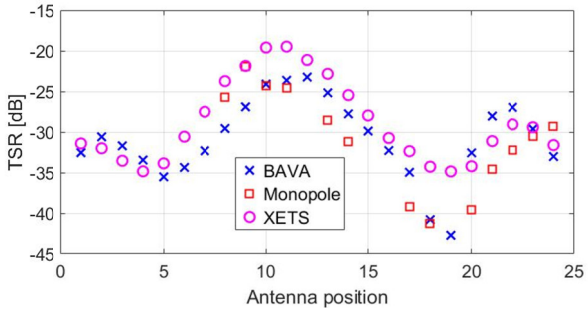

Fig. 18: Tumor-to-skin ratio at different antenna positions for the three antennas considered in this study. The absent markers for the monopole antenna correspond to positions where the feeding cable precludes the detection of the tumor.

Firstly, maximum and minimum TSR are consistent for the three antennas, proving the measurement conditions are similar. The maximum around the 11-th position corresponds to the antenna position that is closest to the tumor and, therefore, maximum energy is retrieved from it. On the contrary, the 19-th position is the farthest and the distance between antenna and tumor suffers the most attenuation, which means that the antenna gets a lower tumor response relative to the skin backscattering.

Secondly, the BAVA and XETS antenna perform similarly, although the latter is more stable. Given that the Vivaldi antenna exhibits better front-to-back ratio, we could have expected that more energy is coupled into the breast. Yet, the results in Fig. 18 prove that this does not necessarily lead to better TSR. Therefore, using a more directive antenna does not lead to larger tumor responses relative to skin backscattering, as both increase by approximately the same factor.

Finally, concerning the monopole, the TSR results are not conclusive, because the cable effect prevents the detection of the tumor at several positions.

B. Discussion of impact of the proposed antenna characterization

To demonstrate the effectiveness of the propose strategies, we imaged the breast using each of the three antennas, using the algorithms briefly presented in Section IV A and B. The artifact removal was implemented considering N_n = 2 and the useful frequency points were restricted to Δf = [2, 5] GHz in a total of N_f = 34 frequency points. We also computed the imaging metrics detailed in Section IV C, in order to assess the improvement in the tumor detection. Lastly, the tumor was placed at coordinates (x_t, y_t, z_t) of (-10, -5, -32) mm.

The imaging results based on experimental data obtained using all the strategies discussed in previous sections are illustrated in Fig. 19 for the three antennas. The results represented in the figure, correspond to z and x planes where maximum intensity was achieved. The elliptical white contour marks the tumor container, whereas the exterior white contour defines the limits of the breast phantom. In the case where the tumor container is not marked, the maximum intensity was obtained for a lower value of z.

This article has been accepted for publication in a future issue of this journal, but has not been fully edited. Content may change prior to final publication. Citation information: DOI 10.1109/TAP.2019.2905742, IEEE Transactions on Antennas and Propagation

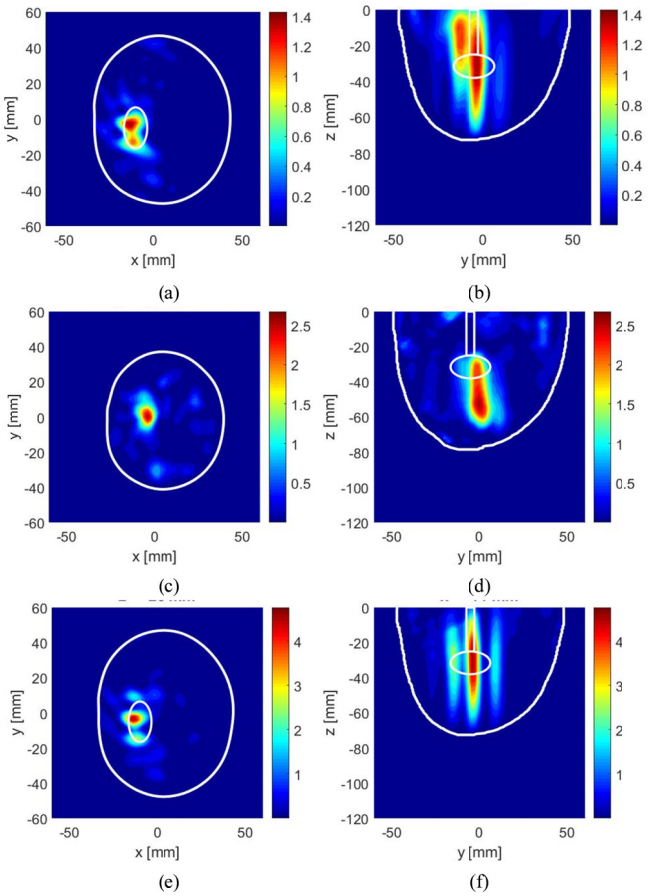

Fig. 19: Imaging results of the breast obtained with each antenna included in this study: (a) and (b) image planes at z = -30 mm and x = 14 mm, respectively, using BAVA; (c) and (d) image planes at z = -54 mm and x = -4 mm, respectively, using monopole; (e) and (f) image cuts at z = -28 mm and x = 14 mm, respectively, using XETS. The white contours identify the breast limits and the tumor container.

When all the antenna-characterization techniques are used, the tumor is correctly detected with the three antennas. Although the monopole presents the feeding problems discussed throughout this work, it still manages to detect the tumor, despite the error in its z coordinate. The detection is reasonably good with TCR of 5.7 dB, 2.2 dB and 2.3 dB for the BAVA, monopole and XETS antennas, respectively. The tumor retrieved image is elongated along the z-axis due to the lack of resolution in this direction, which results from the few measurement planes along z. TABLE VI summarizes the remaining imaging metrics calculated for each antenna.

TABLE VI

CALCULATED IMAGING METRICS USING ALL THE ANTENNA-CHARACTERIZATION STRATEGIES.

Antenna	***BAVA***	***Monopole***	***XETS***
Positive detection	Yes	Yes	Yes
Detected (x_t, y_t, z_t) [mm]	(14,-4,-30)	(-4,0,-54)	(-14,-4,-28)
Intensity, T	1.43	2.67	4.76
TCR [dB]	5.7	2.2	2.3
TMR [dB]	13.1	11.8	13.9
PE [mm]	16	24	5

In order to analyze the importance of the antenna-characterization techniques, we imaged the breast with the three antennas while excluding one of the discussed corrections at a time. For conciseness, we only show the imaging results obtained with the XETS. Nevertheless, the metrics are summarized for all antennas in TABLE VII.

TABLE VII

Calculated imaging metrics when one of the antenna-characterization strategies is not used, while the other are considered.

	BAVA		
Strategy not used	Free-space subtraction	$\Delta\rho(\theta, \phi)$ calibration	Offset length calibration
Positive detection	Yes	Yes	No
Detected (x_t, y_t, z_t) [mm]	(-4,0,-14)	(-12,2,-32)	-
Intensity, T	17.39	1.39	-
TCR [dB]	3	5.5	-
TMR [dB]	11.3	12.9	-
PE [mm]	19	4	-

	Monopole antenna		
Strategy not used	Free-space subtraction	$\Delta\rho(\theta, \phi)$ calibration	Offset length calibration
Positive detection	Yes	Yes	No
Detected (x_t, y_t, z_t) [mm]	(2,-16,-32)	(-4,2,-54)	-
Intensity, T	1.33	2.73	-
TCR [dB]	1.37	2.73	-
TMR [dB]	9.6	10.4	-
PE [mm]	16	12	-

	XETS antenna		
Strategy not used	Free-space subtraction	$\Delta\rho(\theta, \phi)$ calibration	Offset length calibration
Positive detection	No	Yes	No
Detected (x_t, y_t, z_t) [mm]	-	(-14,-4,-28)	-
Intensity, T	-	4.75	-
TCR [dB]	-	2.1	-
TMR [dB]	-	13.6	-
PE [mm]	-	5	-

Let us start by studying the imaging results when $S^{fs}(f)$ is not subtracted prior to the artifact removal execution. Recall that this strategy has been proved to be extremely relevant, because it removes the antenna internal reflections, thus allowing correctly identifying the skin backscatter. The imaging results with the XETS are shown in Fig. 20.

This article has been accepted for publication in a future issue of this journal, but has not been fully edited. Content may change prior to final publication. Citation information: DOI 10.1109/TAP.2019.2905742, IEEE Transactions on Antennas and Propagation

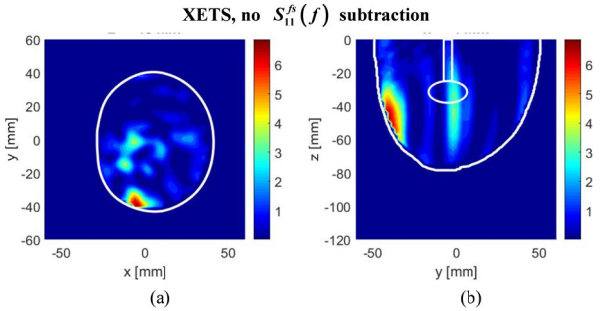

Fig. 20: Imaging results of the breast obtained with the XETS when free-space input reflection coefficient is not subtracted to the measured signals prior to artifact removal execution: (a) z = -48 mm; (b) x = -4 mm. The white contours identify the breast limits and the tumor container.

It is evident that there is a deterioration of the results, since the tumor is not detected. The imaging deterioration is also verified for the BAVA and monopole antennas (see TABLE VII). This is easily explained by the poor performance of the artifact removal. We note that most artifact removals in the literature rely on the accurate identification of the skin backscattering. Therefore, these results should not be only expectable with the present algorithm, but rather with most algorithms.

We now analyze how the imaging results improve when the angular variation of the pseudo near-field phase center, $\Delta d_\rho(\theta, \phi)$, is not compensated. The results using XETS are illustrated in Fig. 21.

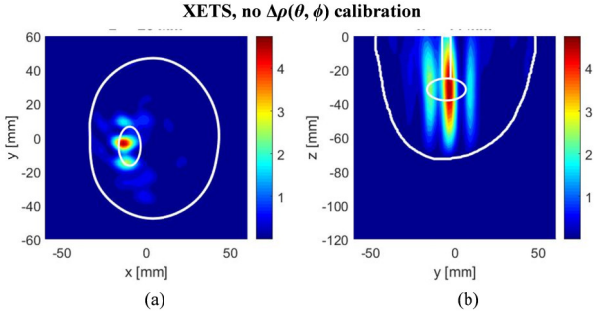

Fig. 21: Imaging results of the breast obtained with the XETS when the variation of the near-field phase center with angle, $\Delta\rho(\theta, \phi)$, is not calibrated: (a) z = -28 mm; (b) x = -14 mm. The white contours identify the breast limits and the tumor container.

In order to grasp the improvement obtained with the compensation of the "near field phase center", the results in Fig. 21 should be compared with the ones in Fig. 19 (alternatively, the reader may compare TABLE VI and TABLE VII). Focusing on TCR we notice slight improvement of 0.2 dB using the XETS. With the monopole the benefit of calibrating the angular dispersion of the "near-field phase center" is more evident, since it presents the greatest dispersion of the three antennas (Fig. 13 (b)). These results indicate that the prior calibration of the pseudo phase center and its angular dispersion may indeed be used to improve the quality of the final image.

Lastly, we evaluated the impact of not calibrating the offset length introduced by the antenna. The imaging results with the XETS are presented in Fig. 22.

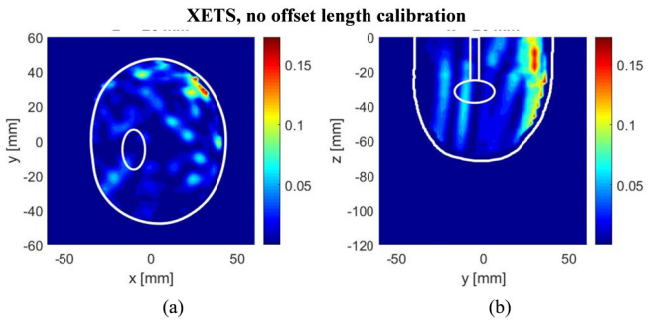

Fig. 22: Imaging results of the breast obtained with the XETS when offset length introduced by the antenna is not calibrated: (a) z = -26 mm; (b) x = 26 mm. The white contours identify the breast limits and the tumor container.

In the absence of this calibration, the energy does not focus and, therefore, the tumor is not detected. In fact, this was verified with all three antennas (see TABLE VII). These results demonstrate the importance of characterizing the antenna used for MMWI.

From these results we conclude that BAVA and XETS present similar imaging performance under the same conditions. Yet, the monopole is much more susceptible to any slight modification in the measurement setup, particularly if there are intense currents on the feeding cable.

Lastly, we note that although we have illustrated our methods using a system that does not require immersion liquid, the methods are also suitable for systems that use contact liquid. In these cases, the antennas must be characterized inside the same liquid as the one intended for the examination, in the absence of any backscatterer that might introduce clutter in the signals.

VII. Conclusion

Microwave imaging has shown great potential for biomedical applications, such as breast cancer screening or brain hemorrhage detection. One of the elements with most influence on the performance of the overall system is the antenna. In fact, as a non-ideal element, it introduces distortion and clutter to the measured signals. Here, we show how to take advantage of proper antenna calibration, as to improve the imaging performance of the overall system. To this end, we perform a detailed study of the antennas and remove some of the adverse effects introduced by it. Although the study is based on experimental signals that were measured using the microwave breast imaging setup we have developed, the results can be extended to other MMWI applications.

Firstly, we demonstrated that subtracting the free-space input reflection coefficient to the signals in the presence of the body is effective in reducing the internal reflections occurring inside the antenna structure. Moreover, we showed that this strategy introduces near-zero distortion to the backscatters originated inside the body. This conclusion is valid, as long as the antenna is immune to the presence of the body, which we proved is reasonably true.

Secondly, we proposed a technique to determine that average near-field phase center along frequency, based on a planar acquisition data set. From the same measurement setup, we characterized the dependence of the phase center on the angle of incidence.

The third calibration procedure we have addressed concerns the offset distance introduced by the propagation of currents. This is absolutely essential in MWI systems, since it directly affects the focusing of the imaging algorithm, which involves distance calculations. Moreover, we showed that the offset distance exhibits dependence on frequency. The proposed calibration method consists of measuring the transmission coefficient of the antennas from which the offset length is inferred.

We applied the calibration strategies to three antenna topologies (BAVA, planar monopole and slot-based antennas) and imaged the breast. The results show very good focusing by all three antennas, proving the calibration methods are effective and do not influence the tumor response. We have demonstrated that the calibration strategies improve the image quality significantly. In fact, we showed that removing the internal reflections of the antenna is absolutely essential and so is the calibration of the equivalent length introduced by the currents for the imaging focusing. Moreover, we proved that the angular characterization of the "phase center" is an effective technique to take advantage of prior knowledge about the antenna and improve the image focusing. Lastly, the results suggest that the proposed techniques are effective when applied to any antenna, if the latter exhibits coherent performance in the presence of the body. This last point is extremely important, since, as we have shown, the imaging results are significantly affected by the feeding cable, as was the case of the monopole. Lastly, the balanced structure of the XETS antenna presented slightly better imaging results, although the dimensions of the XETS do not allow stacking as many sensors around the breast, as would be desired. We plan to extend the methods presented here to multistatic systems.

ACKNOWLEDGMENT

The authors are grateful to António Almeida for his collaboration in the measurements and to Jorge Farinha and Carlos Brito for the setup and prototypes manufacturing.

REFERENCES

[1] E. C: Fear, X. Li, S. C. Hagness, and M. A. Stuchly, "Confocal microwave imaging for breast cancer detection: localization of tumors in three dimensions," *IEEE Trans. Biomed. Eng.*, vol. 49, no. 8, pp. 812-822, Aug. 2002.

[2] E. J. Bond, X. Li, S. C. Hagness, and B. D. V. Veen, "Microwave imaging via space-time beamforming for early detection of breast cancer," *IEEE Trans. Antennas Propag.*, vol. 51, no. 8, pp. 1690-1705, Aug. 2003.

[3] M. Klemm, J. A. Leendertz, D. Gibbins, I. J. Craddock, A. Preece, and R. Benjamin, "Microwave radar-based differential breast cancer imaging: imaging in homogeneous breast phantoms and low contrast scenarios," *IEEE Trans. Antennas Propag.*, vol. 58, no. 7, July 2010.

[4] A. T. Mobashsher, A. M. Abbosh, and Y. Wang, "Microwave system to detect traumatic brain injuries using compact unidirectional antenna and wideband transceiver with verification on realistic head phantom," *IEEE Trans. Microw. Theory Techn.*, vol. 62, no. 9, pp. 1826-1836, Sep. 2014.

[5] Y. Wang, A. M. Abbosh, B. Henin, and P. T. Nguyen, "Synthetic bandwidth radar for ultra-wideband microwave imaging systems," *IEEE Trans. Antennas Propag.*, vol. 62, no. 2, pp. 698-705, Feb. 2014.

[6] A. T. Mobashsher, and A. M. Abbosh, "Performance of directional and omnidirectional antennas in wideband head imaging," *IEEE Antennas Wireless Propag. Lett.*, vol. 15, pp. 1618-1621, 2016.

[7] J. Liang, C. C. Chiau, X. Chen, and C. G. Parini, "Study of a printed circular disc monopole antenna for UWB systems," *IEEE Trans. Antennas Propag.*, vol. 53, no. 11, pp. 3500–3504, Nov. 2005.

[8] X. Yun, E. C: Fear, and R. H. Johnston, "Compact antenna for radar-based breast cancer detection," *IEEE Trans. Antennas Propag.*, vol. 53, no. 8, pp. 2374-2380, Aug. 2005.

[9] C. H. See, R. A. Abd-Alhameed, S. W. J. Chung, D. Zhou, H. Al-Ahmad, and P. S. Excell, "The design of a resistively loaded bowtie antenna for applications in breast cancer detection systems," *IEEE Trans. Antennas Propag.*, vol. 60, no. 5, pp. 2526-2530, May 2012.

[10] A. T. Mobashsher, an A. M. Abbosh, "Compact 3-D slot-loaded folded dipole antenna with unidirectional radiation and low impulse distortion for head imaging applications," *IEEE Trans. Antennas Propag.*, vol. 64, no. 7, pp. 3245-3250, July 2016.

[11] E. Porter, H. Bahrami, A. Santorelli, B. Gosselin, L. A. Rusch, and M. Popovic, "A wearable microwave antenna array for time-domain breast tumor screening," *IEEE Trans. Med. Imag.*, vol. 35, no. 6, pp. 1501-1509, June 2016.

[12] T. Sugitani, S. Kubota, A. Toya, X. Xiao, and T. Kikkawa, "A compact 4x4 planar UWB antenna array for 3-D breast cancer detection," *IEEE Antennas Wireless Propag. Lett.*, vol. 12, pp. 733-736, 2013.

[13] D. Gibbins, M. Klemm, I. J. Craddock, J. A. Leendertz, A. Preece, and R. Benjamin, "A comparison of a wide-slot and a stacked patch antenna for the purpose of breast cancer detection," *IEEE Trans. Antennas Propag.*, vol. 58, no. 3, pp. 665-674, March 2010.

[14] J. Bourqui, M. Okoniewski, and E. C. Fear, "Balanced antipodal Vivaldi antenna with dielectric director for near-field microwave imaging," *IEEE Trans. Antennas Propag.*, vol. 58, no. 7, pp. 2318-2326, July 2010.

[15] F. Yang, and A. S. Mohan, "Microwave imaging for breast cancer detection using Vivaldi antenna array," *International Symposium on Antennas and Propagation 2012 (ISAP 2012)*, pp. 1-4, Nov. 2012, Nagoya, Japan.

[16] R. K. Amineh, M Ravan, A. Trehan, and N. K. Nikolova, "Near-field microwave imaging based on aperture raster scanning with TEM horn antennas," *IEEE Trans. Antennas Propag.*, vol. 59, no. 3, pp. 928-940, Mar. 2011.

[17] J. Sachs, M. Helbig, S. Ley, P. Rauschenbach, M. Kmec, and K. Shilling, "Short interfacial antennas for medical microwave imaging," *Antenna Technology: Small Antennas, Innovative Structures, and Applications (iWAT), 2017 International Workshop on*, pp. 1-4, Mar. 2017.

[18] B. Maklad, *et al.*, "Neighborhood-based algorithm to facilitate the reduction of skin reflections in radar-based microwave imaging," *Progress In Electromagnetics Research B*, Vol. 39, pp. 115-139, 2012.

[19] M. J. Burfeindt, T. J. Colgan, R. O. Mays, J. D. Shea, N. Behdad, B. D. V. Veen, and S. C. Hagness, "MRI-derived 3-D-printed breast phantom for microwave breast imaging validation," *IEEE Antennas Wireless Propag. Lett.*, vol. 11, pp. 1610-1613, 2012.

[20] J. M. Felício, J. R. Costa, and C. A. Fernandes, "Complex permittivity and anisotropy measurement of 3D-printed PLA at microwaves and millimeter-waves," *International Conference on Applied Electromagnetics and Communications (ICECOM 2016)*, pp. 1-6, Dubrovnik, Croatia, 2016.

[21] N. Joachimowicz, C. Conessa, T. Henriksson, and B. Duchêne, "Breast phantoms for microwave imaging," *IEEE Antennas Wireless Propag. Lett.*, vol. 13, pp. 1333-1336, 2014.

[22] G. G. Rayleigh, and J. M. Cioffi, "Spatio-temporal coding for wireless communications," *Global Telecommunications Conference, 1996. GLOBECOM '96. 'Communications: The Key to Global Prosperity*, pp. 1809-1814, Nov. 1996, London, UK.

[23] (Feb. 2018). *CST – Computer Simulation Technology* [Online]. Available: www.cst.com.

[24] P. J. Gibson, "The Vivaldi aerial," *Proc. IEEE 9th Eur. Microw. Conf*, 1979, pp. 101–105.

[25] K. Kikuta, and A. Hirose, "Compact folded-fin tapered slot antenna for UWB applications," *IEEE Antennas Wireless Propag. Lett.*, vol. 14, pp. 1192-1195, 2015.

[26] J. H. Lu, and C. H. Yeh, "Planar broadband arc-shaped monopole antenna for UWB system," *IEEE Trans. Antennas Propag.*, vol. 60, no. 7, pp. 3091-3095, July 2012.

[27] H. M. Jafari, M. Jamal Deen, S. Hranilovic, and N. K. Nikolova, "A study of ultrawideband antennas for near-field imaging," *IEEE Trans. Antennas Propag.*, vol. 55, no. 4, pp. 1184-1188, April 2007.

[28] M. N. Moghadasi, H. Rousta, and B. S. Virdee, "Compact UWB planar monopole antenna," *IEEE Antennas Wirelles Propag. Lett.*, vol. 8, pp. 1382-1385, 2009.

[29] M. Sun, Y., P. Zhang, and Y. Lu, "Miniaturization of planar monopole antenna for ultrawideband radios," *IEEE Trans. Antennas Propag*, vol. 58, no. 7, pp. 2420-2425, July 2010.

[30] M. Koohestani, N. Pires, A. K. Skrivervik, and A. A. Moreira, "Performance study of a UWB antenna in proximity to a human arm," *IEEE Antennas Wirelless Propag. Lett.*, vol. 12, pp. 555-558, 2013.
[31] L. Liu, S.W. Cheung, Y.F. Weng and T.I. Yuk, "Cable effects on measuring small planar UWB monopole antennas," *Ultra Wideband - Current Status and Future Trends*, Dr. Mohammad Matin (Ed.), InTech, 2012.
[32] J. R. Costa, C. R. Medeiros, and C. A. Fernandes, "Performance of a crossed exponentially tapered slot antenna for UWB systems," *IEEE Trans. Antennas Propag.*, vol. 57, no. 5, pp. 1345-1352, May 2009.
[33] C. A. Fernandes, J. R. Costa, E. B. Lima, and M. G. Silveirinha, "Review of 20 years of research on microwave and millimeter-wave lenses at 'Instituto de Telecomunicações'," *IEEE Antennas Propag. Mag.*, vol. 57, no. 1, pp. 249–268, Feb. 2015.

João M. Felício (S'14) was born in Lisbon, Portugal, in 1990. He received the Licenciado and Master degrees in Electrical and Computer Engineering from the Instituto Superior Técnico (IST), University of Lisbon, Lisbon, Portugal, in 2013 and 2014, respectively.
He is currently working towards his PhD at IST, Lisbon, Portugal, while doing research at Instituto de Telecomunicações, Lisbon. His main interests include Microwave Imaging, antenna design and antennas for biomedical applications.

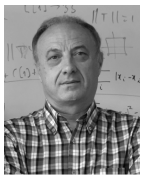

José M. Bioucas-Dias (S'87–M'95–SM'15–F'17) received the EE, MSc, PhD, and Habilitation degrees in electrical and computer engineering from Instituto Superior Técnico (IST), Universidade Técnica de Lisboa (now Universidade de Lisboa), Portugal, in 1985, 1991, 1995, and 2007, respectively. Since 1995, he has been with the Department of Electrical and Computer Engineering, IST, where he is a Professor and teaches inverse problems in imaging and electric communications. He is also a Senior Researcher with the Pattern and Image Analysis group of the Instituto de Telecomunicações, which is a private non-profit research institution.
His research interests include inverse problems, signal and image processing, pattern recognition, optimization, and remote sensing. He has introduced scientific contributions in the areas of imaging inverse problems, statistical image processing, optimization, phase estimation, phase unwrapping, and in various imaging applications, such as hyperspectral and radar imaging. He was included in Thomson Reuters' Highly Cited Researchers 2015 list and received the IEEE GRSS David Landgrebe Award for 2017.

Jorge R. Costa (S'97–M'03–SM'09) was born in Lisbon, Portugal, in 1974. He received the Licenciado and Ph.D. degrees in electrical and computer engineering from the Instituto Superior Técnico (IST), Technical University of Lisbon, Lisbon, Portugal, in 1997 and 2002, respectively.
He is currently a Researcher at the Instituto de Telecomunicações, Lisbon, Portugal. He is also an Associate Professor at the Departamento de Ciências e Tecnologias da Informação, Instituto Universitário de Lisboa (ISCTE-IUL). His present research interests include lenses, reconfigurable antennas, MEMS switches, UWB, MIMO and RFID antennas. He is the coauthor of four patent applications and more than 150 contributions to peer reviewed journals and international conference proceedings. More than thirty of these papers have appeared in IEEE Journals. Prof. Costa served as an Associate Editor for the IEEE Transactions on Antennas and Propagation from 2010 to 2016 and he was a Guest Editor of the Special Issue on "Antennas and Propagation at mm- and Sub mm-Waves", from the IEEE Transactions on Antennas and Propagation, April 2013. He was the Co-Chair of the Technical Program Committee of the European Conference on Antennas and Propagation (EuCAP 2015) in Lisbon and General Vice-Chair of EuCAP 2017 in Paris.

Carlos A. Fernandes (S'86–M'89–SM'08) received the Licenciado, MSc, and PhD degrees in Electrical and Computer Engineering from Instituto Superior Técnico (IST), Technical University of Lisbon, Lisbon, Portugal, in 1980, 1985, and 1990, respectively. He joined IST in 1980, where he is presently Full Professor at the Department of Electrical and Computer Engineering in the areas of microwaves, radio wave propagation and antennas. He is a senior researcher at the Instituto de Telecomunicações and member of the Board of Directors. He has co-authored a book, 2 book chapter, more than 180 technical papers in peer reviewed international journals and conference proceedings and 7 patents in the areas of antennas and radiowave propagation modeling. His current research interests include dielectric antennas for millimeter wave applications, antennas and propagation modeling for personal communication systems, RFID and UWB antennas, artificial dielectrics and metamaterials. He was a Guest Editor of the Special Issue on "Antennas and Propagation at mm- and Sub mm-Waves", from the IEEE Transactions on Antennas and Propagation, April 2013.